The Use of Digital-Image Correlation to Investigate the Cohesive Zone in a Double-Cantilever Beam, with Comparisons to Numerical and Analytical Models

J. M. Gorman* and M. D. Thouless*,**[1]

*Department of Mechanical Engineering
**Department of Materials Science & Engineering
University of Michigan, Ann Arbor, MI 48109, USA

Abstract

Digital-image correlation (DIC) is used to analyze an adhesively-bonded double-cantilever beam (DCB), and to determine the traction-separation law for a cohesive-zone model. The issues involved with how to extract useful information from the digital data of DIC are addressed. In addition, DIC is used to explore how the cohesive zone evolves, and to determine how the elastic arms deform in response to the loading and to the adhesive. The results of these observations are compared to numerical and analytical models for the DCB geometry. In particular, the well-known concept of root rotation is demonstrated. It is shown that, by combining the effects of shear into an effective root rotation, it is possible to use a simple Euler-beam approximation to describe the compliance of the DCB. The experiments and analysis also illustrate the lesser-known concept that significant compression can occur beyond the tensile region in the cohesive zone ahead of a DCB crack tip. Therefore, for accurate numerical predictions, a cohesive-zone model must incorporate compressive deformation. The DIC results are further used to illustrate the concept of a cohesive-length scale. This is defined in terms of the work done against crack-tip tractions, the opening displacement, the stiffness of the arms, and a characteristic geometrical length. The cohesive-length scale is measured experimentally in this paper, and its magnitude is shown to indicate when linear elasticity can be used to describe the deformation of a DCB geometry. The cohesive-length scale is shown to correlate with both the root rotation and the length of a cohesive zone in a fashion that is very similar to what is predicted analytically by elastic-foundation models. Finally, it is demonstrated that, when used in a cohesive-zone model of the geometry, the experimentally determined traction-separation law gives excellent predictions for the evolution of the cohesive zone and for the deformation of the elastic beams. A very minor discrepancy is associated with in-plane tensile stresses that must develop within an adhesive layer in response to the deformation of the beams.

August 13, 2018

Keywords: Digital-Image Correlation, Double-Cantilever Beam, Cohesive Zone, Root Rotation, Traction-Separation Law

[1]Corresponding author: (001)734-763-5289 (thouless@umich.edu)

1 Introduction

The use of cohesive-zone models has become a standard engineering tool in fracture mechanics, and in the analysis of adhesive joints. Over the past couple of decades many different groups have developed approaches to deducing traction-separation laws, and have implemented these within finite-element models. Generally, validation of these models has focussed on predicting load-displacement curves and failure. Less attention has been focussed on experimental studies of how the cohesive zone interacts with the surrounding structure, and on comparisons of these observations with numerical and analytical predictions. This is the focus of the present study: the use of digital-image correlation to study a cohesive-zone associated with the mode-I deformation of an adhesive layer.

The double-cantilever beam (DCB) geometry has been recognized as a useful geometry for extracting the mode-I fracture and adhesive properties of interfaces since Obriemoff first used it in 1930 to examine the cleavage of mica [1]. The geometry becomes especially useful when loaded by pure moments, because the energy-release rate (or J-integral) is then unaffected by the nature of the bonding across the interface. Therefore, this manifestation of the geometry provides a particularly robust experimental method to extract the mode-I cohesive parameters of composites and adhesives. However, it does rely on the use of a specially designed loading jig [2, 3].

A common variant of the DCB geometry is one that is loaded by opening point forces at the crack mouth [4, 5, 6]. This is a simple configuration to realize experimentally, but leads to analytical complications owing to the introduction of shear [7, 8, 9]. Many approaches have been taken to model the effects of shear in this geometry, using different combinations of analytical and numerical techniques [7, 8, 9, 10, 11, 12, 13, 14, 15, 16]. The mechanics

underlying the different approaches and assumptions used in these analyses have recently been unified by Thouless [17].

While the analysis of a point-loaded DCB specimen would appear to require knowing the position of the crack tip, the geometry is remarkably robust analytically, and a number of modified analytical approaches have been proposed to enable the toughness to be determined without specific measurement of the crack length [18, 19, 20]. However, an alternative, simple, elegant and rigorous result exists to determine the value of the J-integral along an exterior boundary of the DCB geometry by measuring just the applied load per unit width, P_∞, and the relative rotation between the loading points, Θ [21, 22, 23]:

$$J_{ext} = P_\infty \Theta \ . \tag{1}$$

If the normal crack-tip opening displacement, δ_o, is measured simultaneously with J_{ext}, the mode-I traction-separation law for the interface in a purely symmetrical specimen can be calculated from the gradient of a plot of J_{ext} against δ_o [24]:

$$\sigma(\delta_o) = \frac{dJ_{ext}}{d\delta_o} \ . \tag{2}$$

This is probably the simplest way to determine the properties of an interface using a DCB geometry with elastic arms [25, 26, 27], and it will be used in the present paper.

Digital-image correlation (DIC) has become a very common technique for tracking surface displacements, and for calculating the associated surface deformations [28, 29]. The technique involves applying a speckle pattern to the surface of a specimen to produce a non-uniform gray-scale pattern. This pattern is then converted into a digital surface of gray scales (with bi-cubic splines being one common interpolation method used to create a continuous digital surface). The subsequent movements of the peaks and valleys are then

tracked to determine the surface-displacement vectors.

The intent of the present work is to use DIC to determine the mode-I traction-separation law for an adhesive joint, and to explore details of the deformation within the cohesive zone. Previous approaches to extract cohesive parameters using DIC are divided into two groups. In one approach [30, 31], DIC observations are used to obtain displacement and strain maps over an extended region at the crack tip, and then an inverse method is used to back out the traction-separation law by a finite-element analysis. In the second approach [26, 27, 32, 33], DIC is used to determine the opening displacement at the crack tip, and Eqn. 2 is used to compute the traction-separation law directly.

In the present paper, we use the latter approach, but extend the investigation to explore the full deformation of the DCB geometry both ahead of and behind the crack tip. Using this approach, we are able to demonstrate the concepts of root rotation and shear at the crack tip [17], cohesive-length scales [34, 35], the role of the compressive portion of the traction-separation law [36], and any limitations of linking a cohesive zone (rather than continuum elements) in computational models to the deformation ahead of the crack tip. It might be noted that much of what will be shown in this paper about the relationships between a cohesive zone and the deformation of the system could have been developed within an entirely numerical paper. However, here, we illustrate these concepts experimentally, using DIC as a diagnostic tool.

1.1 Cohesive-zone model

The cohesive-zone model (CZM) [37, 38] was originally developed as a numerical tool to study fracture, but it is increasingly becoming a general way to formulate fracture me-

chanics, as it bridges both energy-based and strength-based perspectives [34, 35, 36]. It is within this context that we use a cohesive zone in the current work. We take the approach proposed by Yang *et al.* [39, 40] to replace the entire adhesive layer by a cohesive zone, and to evaluate the effective cohesive law for a particular thickness of the adhesive. We use DIC to deduce the details of the cohesive law. However, the full-field capabilities of DIC provide additional information concerning the deformation of the joints and the use of cohesive-zone models to describe this deformation, which we can explore in detail.

One concept that we will be using in this work is that of the cohesive length, ξ. While this can be defined in a general fashion for any location along an interface under mixed-mode conditions for a bimaterial system [35], here we focus only on its value at the cohesive crack tip for a symmetrical, isotropic DCB specimen. In particular, we define the crack-tip cohesive-length scale as

$$\tilde{\xi}_o = \frac{\xi_o}{h} = \frac{\bar{E}\delta_o^2}{\mathcal{W}_o h} \, . \tag{3}$$

where δ_o is the crack-tip opening displacement, $\mathcal{W}_o$ is the local work done against the mode-I tractions at the crack tip, $\bar{E}$ is the effective modulus of the arms (E in plane stress, or $E/(1-\nu^2)$ in plane strain, where ν is Poisson's ratio), h is the thickness of the DCB arms, and the subscript "o" identifies a value at the cohesive crack tip. If the cohesive-length scale is very small (typically less than about 0.4), then the mechanics can be described as a linear-elastic continuum. If $\tilde{\xi}_o$ is significantly larger than about 1, then the cohesive tractions can have a clearly identifiable effect on the deformation of the structure as a whole. In contrast to similar quantities expressed in terms of failure parameters [37, 41], or a transition crack size, this definition of the cohesive-length scale allows the description of a system to evolve during the loading process.

From the path-independence of the J-integral, one can equate $\mathcal{W}_o$ to J_{ext}. Therefore, the crack-tip cohesive-length scale, $\tilde{\xi}_o$, can be found experimentally during the course of a test from the measured values of J_{ext} and δ_o. This will be demonstrated in the current paper. In particular, the transition between linear and non-linear deformation, and the relationship of the length of the cohesive zone to the magnitude of $\tilde{\xi}_o$ will be described.

2 Experimental Methods

The geometry used for the studies described in this paper is shown in Fig. 1. The two arms of a double-cantilever beam were made from 4.8 mm sheets of 4130 steel, with a yield strength of 340 MPa. The beams were cut to a length of 152 mm, and milled to a uniform width of 21.4 mm. The bonding surfaces of the beams were polished to the level of 100-grit, and a layer of a two-part epoxy (Dow Betamate® 73326M/73327M) was spread on the surface of one beam. Glass spheres with a diameter of $250\,\mu\mathrm{m}$ were sprinkled onto the adhesive, so as to ensure a uniform thickness of the bonding layer. The second beam, upon which a strip of Teflon® tape was placed to create a starter-crack, was put on top of the first beam, aligned, and the system was clamped by binder clips for two days. After the binder clips were removed, the adhesive was cured at room temperature for an additional week, and the sides of the specimen were ground to remove extruded adhesive. Optical observations indicated that the thickness of the resultant adhesive layer was $275 \pm 25\,\mu\mathrm{m}$.

Loading tabs were made from a 3-mm-thick, low-carbon steel, and bonded to the DCB using the same two-part epoxy that formed the adhesive layer. During the test, the load was applied through pin joints in the tabs, with a lubricant being sprayed on the pins to decrease the effects of friction. The dimensions of the tabs were such that the distance from

the loading point to the crack tip, a_o, was 42 mm. After polishing the sides of the DCB with a 600-grit sandpaper, an Iwata™ CM-B airbrush was used to apply a black-and-white speckle pattern to the specimen. Testing was completed within a day of the application of the paint, using a servo-hydraulic test machine (MTS 858 Mini Bionix II™) at a nominal cross-head displacement rate of 1.15 mm/min. Two 5-megapixel Grasshopper™ cameras were used to provide separate, but synchronized, digital images of the region containing the tabs and of the region near the crack-tip. These images were analyzed using the Vic-2D™ software package from Correlated Solutions, Inc. Subset and step sizes of 35 and 3 pixels, respectively, were used for the analysis.

Initial attempts to rely on a purely digital approach to analyze the data, using the internal software of the DIC system to deduce strains and rotations, resulted in excessive noise. With a beam-like geometry, such as that used in this study, the displacement vectors vary in a linear fashion perpendicular to the length of the beam. Therefore, an analogue approach to the data analysis was adopted. The relevant portions of the displacements were plotted as linear functions, and the slopes of the resultant lines were used to determine the rotation and strain components. As may be seen from some of the displacement plots provided in the following sections, this approach allows one to identify and treat appropriately the portions of data that are obviously numerical artifacts.

3 Results

3.1 Measurement of traction-separation law

The DIC analysis in this work proceeded by plotting displacement components along lines, and then using these plots to deduce strains and rotations by means of linear regressions,

rather than relying on the direct output of the commercial software. The color map (shown in Fig. 2a) shows an example of the color-coded vertical displacements in the loading region beneath the tabs on the top beam, for one particular load. This color map contains displacement data from more than 4000 data points. When plotted as a function of axial distance along the beam, all these data points collapse to a single line. This is illustrated in Fig. 2b for five distinct loads, A-E, defined in Fig. 3. The slopes of these lines give the rotations of the beam at different loads.[2] When combined with an equivalent analysis of the bottom beam, the relative rotation between the two loading points, Θ, can be determined, and plotted against the corresponding load, as in Fig. 3. Although the data may look approximately linear between the loads labelled "A" and "D", it will be shown later that true linear-elastic behavior of this specimen was limited to the small linear region that can be seen below the point "A", at loads less than about 1 N/mm.

It is noted that the rotations were measured under loading tabs that extended over a distance $l = 7$ mm to both sides of the loading point. Therefore, the assumption in the derivation of the J-integral that the load is applied at a point is not strictly valid. This issue can be finessed by recognizing that, just beyond the loading tabs, the measured rotation will still be correct, but the arms will be acted upon by a transverse shear load of P_∞ and a bending moment of $P_\infty l$. The J integral can then be computed as $J = P_\infty\Theta + 12(P_\infty l)^2/\bar{E}h^3$. However, in the present experiment, the correction that this implies is negligible.

The location of the crack tip could be determined directly from its surface trace after a small increment of loading, and the corresponding location then identified in the images taken at lower loads. The location was also confirmed by the point where image correlation was lost [42]. However, although the thickness of the adhesive layer was known, the

[2]The contribution of shear to this rotation is sufficiently small to be neglected.

position of the layer was concealed by the speckle pattern. This problem was addressed by measuring the vertical displacements, w, relative to an arbitrary reference point, as a function of vertical position, z, along a line passing through the crack-tip (Fig. 4a). As shown in a plot of the relative displacements and position (Fig. 4b), there was a dramatic change in normal strain $\varepsilon_{zz} = \partial w/\partial z$ between the steel and adhesive, allowing the opening displacement across the adhesive layer to be determined.

The strain within the adhesive is not represented accurately by the data of Fig. 4b. This is because the apparent region of enhanced strain does not correspond to the actual thickness of the adhesive layer. The jump in displacements that occurs across the adhesive layer is smoothed out by the algorithm used by the DIC software to compute displacements. In the present case, the transition extends about 150 μm beyond the actual interfaces between the steel and adhesive. The extent of the transition region is dependent on the choice of the pixel subset used by the DIC software, with there being a balance between an increased noise associated with a small subset against an increased transition width associated with a larger subset.

Although the DIC data cannot be used to compute the thickness of the adhesive layer, the opening displacements across the interface can be measured accurately from the displacement values just outside the transition region, since the strain in the steel is very small. In a test with more compliant arms than steel, one might need to use linear extrapolations of the displacement data to the assumed locations of the interfaces. It should be noted that, owing to the use of local, subset-based DIC, any digital approach that involves direct measurement of the displacements over only the 275 ± 25 μm known to correspond to the thickness of the adhesive would be seriously in error. However, the problems associated with interfacial smoothing might be ameliorated by the use of extended digital-image cor-

relation (X-DIC), which can accommodate displacement discontinuities [43, 44].

The calculations to determine the crack-tip opening were done for the entire sequence of images collected during the test. These calculations included minor corrections to compensate for any effects of rigid-body rotation on the measurements of the relative vertical displacements. In particular, using a co-ordinate system with the x-axis along the interface, and the z-axis normal to the interface and directed from the interface to the surface. the crack-tip opening, was computed as the difference in the normal displacements across the interface:

$$\delta_o = \Delta w' \cos\phi + \Delta u' \sin\phi + t \sin\phi \tag{4}$$

where $\Delta w'$ and $\Delta u'$ are the measured differences in displacements across the interface along the z-axis and x-axis, ϕ is the rigid-body rotation about the y-axis. and t is the thickness of the interface. However, in this particular case, the correction was smaller than the experimental uncertainty.

The corresponding load and relative rotation (Fig. 3) were used to calculate J_{ext} from Eqn. 1. The resultant plot of J_{ext} against crack-tip opening is shown in Fig. 5. It should be noted that the work done against crack-tip tractions, $\mathcal{W}_o$, is identically equal to J_{ext}. Therefore, the data of J_{ext} and crack-tip opening, δ_o, can be combined with the elastic modulus[3] of the steel to compute cohesive-length scales $\tilde{\xi}_o$. Specific values of $\tilde{\xi}_o$ have been added to the points identifying loads "A"-"E". Even at the lowest identified load, "A", the value of $\tilde{\xi}_o$ is larger than the value for which results from linear elasticity are considered to be usefully valid. This will become more obvious in subsequent sections.

[3]The specific value appropriate for this system was determined by a study described in a subsequent section.

As noted on Fig. 5, the crack was observed to begin propagating along the surface before J_{ext} reached a constant value. This indicates that the crack was not propagating uniformly across the width of the specimen. After testing was complete, it was noted that a thin (< 0.5 mm) layer of adhesive failure at the steel-adhesive interface had occurred at the surface while the rest of the specimen failed cohesively. This highlights a limitation of digital-image correlation: DIC only picks up surface measurements, and nothing is known about what is happening through the thickness. However, for the purposes of this study we proceeded on the assumption that the displacements measured at the surface gave reasonable approximations to those in the interior.

Differentiation of the data shown in Fig. 5 gives the mode-I traction-separation law, as described by Eqn. 2. The differentiation required to obtain this law was done by developing a piecewise, polynomial, fitting scheme with continuous derivatives to broad sections of the data. The resultant law is plotted in Fig. 6.[4] As with all differentiation of digital data, the precise details of the resultant law are sensitive to the choice of fitting functions; a representative error bar on Fig. 6 indicates the resultant uncertainty in the stress levels. In particular, it is noted that an analogue approach (also known as "a ruler") to differentiating the data shown in Fig. 5 might have suggested that the points "C" and "D" are connected by a straight line. This would correspond to a broad flat peak of about 13 MPa over about 25 μm. However, such a feature could not be reproduced by the standard curve-fitting algorithms of digital approaches. The portion of the traction-separation law obtained when the surface crack was propagating has been indicated by a dashed line in Fig. 6 to emphasize its tentativeness.

[4]The cohesive strength illustrated in Fig. 6 is somewhat higher than the maximum stress obtained in a experiment where a small bonded joint was loaded in direct tension. However, DIC showed that the deformation in this latter experiment was not completely uniform. Therefore, the fact that a lower value was obtained is consistent with the results obtained from the DCB.

Although the results for only one specimen have been reported in this paper, the experiments were repeated for several different specimens. The results were all similar and consistent, but with about 10% variation in the steady-state toughness between specimens. This additional uncertainty for the mode-I traction-separation law, associated with specimen-to-specimen variability, will be included in subsequent work on mixed-mode fracture. However, accounting for this additional source of variability was not required for the purposes of this present paper. Therefore, the different analyses that are described have all been performed on a single specimen with the particular traction-separation law given in Fig. 6.

3.2 Root rotation

The arms of a DCB are subjected to both shear and rotation at the crack tip [7]. The rotation is associated with the fact that the material ahead of the crack tip is elastic, and the arms of the DCB are not clamped rigidly at the crack tip. The shear is associated with the resultant shear force arising from the applied loads. The net effect of these two phenomena is a relative rotation between the two centroidal axes of the arms at the crack tip, which is termed the *root rotation*. The root rotation increases with the cohesive-length scale, as will be shown in a subsequent section, with a limiting value in the case of perfect bonding along an interface ($\tilde{\xi}_o = 0$) [17].

The full-field measurement capabilities of DIC allow the root rotation to be measured. This can be done by using the same vertical line used to compute crack-tip openings (Fig. 4), but now measuring the horizontal displacements as a function of distance along the vertical line. The resultant data are plotted in Fig. 7(a) for the five loads "A"-"E". These data are the raw data, and have not been corrected for any rigid-body rotations that occur

during loading. The root rotation can be found from the relative rotations between the two arms. It is clear that an assumption of uniform rotation is appropriate outside the interface region, although some fine structure associated with numerical interpolation of the data can be observed for some of the lines. Again, these interpolation artifacts emphasize the need for caution against simple digital differentiation.

The root rotation can be computed without any correction for rigid-body rotations. However, in the interests of visualization, the data of Fig. 7(a) have been replotted in Fig. 7(b) with two modifications. The first is a rotational correction to ensure that the rotations in both arms are symmetrical. The second is a translational correction to set the reference point for zero displacement to be the point where the extrapolated lines from both beams intersect. It appears that this point is not quite in the middle of the region of what might be identified as the interface region containing spurious data associated with loss of correlation.

The relative rotation between the vertical lines at the crack tip for the two arms is plotted as the root rotation, θ_o, against load in Fig. 8. It should be emphasized that the root rotation is defined here as the sum of $\partial u/\partial z$ for each arm (where the z axis for each arm points away from the interface), so the effects of any shear are included in this definition. As shown in Ref. [17], this provides an elegant way of describing root rotation in a fashion that allows one to use Euler-Bernoulli beam theory to describe the compliance of a DCB. This point will be further elaborated upon in the following section. The predicted small-scale root rotation from LEFM, which is $\theta_o = P_\infty(5.44 + 16.2a_o/h)/\bar{E}h$, where the value of $\bar{E}$ was taken to be 217 GPa (see Section 3.3) [17], is also plotted on Fig. 8b.

At very low loads (before point "A"), the rotation calculated from LEFM appears to

describe the root-rotation measurements adequately. This is consistent with the notion that the cohesive-length scale in that low-load regime is near the LEFM limit. However, after point "A", the cohesive-length scale is too large for LEFM results to be valid, and the root rotation is not described by the linear-elastic solution.

3.3 Elastic modulus

From a fracture-mechanics perspective, one can incorporate any effects of shear at the crack tip into an effective root rotation [17]. The compliance of a DCB specimen can then be described by simple Euler-Bernoulli theory, provided the root rotation and root displacement[5] are incorporated as boundary conditions. In the present work, the presence of relatively rigid tabs prevented this concept from being verified at the crack mouth where the load was applied. Therefore, the crack opening was evaluated at an intermediate point situated at a distance $a = 28.3$ mm behind the crack tip. The analysis then needs to recognize that this point is subjected to a transverse shear force, P_∞, and a moment, $M_\infty = P_\infty(a_o - a)$, so that the total crack opening at this location is given by [17]

$$\Delta = 8\frac{P_\infty a^3}{\bar{E}h^3} + 12\frac{P_\infty(a_o - a)a^2}{\bar{E}h^3} + \theta_o a + \delta_o \ . \tag{5}$$

Different values of $\bar{E}$ were used to fit the full range of data, and the best fit is shown in Fig. 9(a). This fit was sensitive to the choice of modulus, to within 2 GPa. However, including the uncertainty of the experimental data, the best fit appeared to be $\bar{E} = 217 \pm 9$ GPa. It will be observed that this fit describes the crack opening very well over the entire range of loads, including all the non-linear portions. As a comparison, a tensile test of the

[5]Strictly speaking, the *root displacement* is the separation between the centroidal axes at the crack tip [17]. However, in the present case, it was determined that the difference between the root displacement and the crack-tip opening was negligible, so δ_o was used in the calculations.

steel using both an extensometer and DIC resulted in a Young's modulus of 204 ± 8 GPa, and a Poisson's ratio of 0.32 ± 0.07. This suggests that the bending modulus determined in Fig. 9(a) falls between the plane-stress and plane-strain values.

Superimposed on the plot of Fig. 9 is the opening that would be predicted for a linear elastic system, with perfect bonding along the interface. This can be computed from the results for the compliance of a linear-elastic DCB given in Ref. [17] as

$$\Delta = \frac{P_\infty}{\bar{E}} \left[8\frac{a^3}{h^3} + 12\frac{(a_o - a)a^2}{h^3} + 16.2\frac{a_o a}{h^2} + 5.44\frac{(a_o + a)}{h} + 3.66 \right] \tag{6}$$

As with the root-rotation measurements, the elastic compliance adequately describes the crack-mouth opening displacement until point "A", at which point the cohesive-length scale is too large for LEFM results to be valid.

Figure 9(b) shows how the opening displacement between the two centroidal axes of the arms varies with distance from the crack tip at the specific load designated by "D". This is compared with the predictions for the profile based on Euler-beam theory, with the boundary conditions for root rotation and root displacement at the crack tip given by the measured values. It was assumed that there was a combined transverse shear force and bending moment at a distance $a = 28.3$ mm behind the crack tip, and the modulus was 217 GPa. There is excellent agreement between the analytical results and and the experimental observations, confirming the notion that it is appropriate to describe the deformation of a DCB by Euler-beam theory, with an appropriate root rotation and root displacement at the crack tip [17].

3.4 Cohesive-zone measurement

While crack-tip displacements are required to deduce traction-separation laws, DIC provides the additional ability to monitor the displacements along the interface ahead of a crack tip, and to investigate how the cohesive zone evolves during loading. This can be done by determining the opening displacements along lines perpendicular to the interface, as illustrated in Fig. 10(a). As an illustration, the relative normal openings along a series of lines 4 mm apart at load "D" are shown in Fig. 10(b). These raw data have not been corrected for any rigid-body rotation of the specimen. However, this correction was made as the data were processed for presentation in the following figures.

Similar sets of data were analyzed all along the bonded interface to obtain the distribution of opening displacements as a function of distance ahead of the crack tip. The results are plotted in Fig. 11. The measurement uncertainty in these plots is about 1 μm ($\sim$0.1 pixel), so the opening data shown for load "A" are close to the limit imposed by the noise. However, the evolution of the cohesive-zone as the applied load is increased can be seen very clearly in this figure.

Figure 11 illustrates the fact that there is ambiguity about how one defines the length of a cohesive zone, because there can be a significant region of compressive loading. Indeed, it is only in an idealized case when the tractions are embedded behind a singular crack tip that a cohesive zone has an unambiguous length. This is one reason why the concept of a crack-tip cohesive length, as defined in Eqn. 3, is considered to be a more useful quantity for describing the mechanics of fracture than the cohesive-zone length. However, it is useful to have some understanding of how the cohesive zone evolves with $\tilde{\xi}_o$.

The distance ahead of the crack tip at which the normal tractions become compressive is plotted as a function of the crack-tip cohesive-length scale, $\tilde{\xi}_o = \xi_o/h$, in Fig. 12(a). As a point of comparison, it is noted that a result related to a linear cohesive law can be obtained analytically from a model of a beam on an elastic foundation, as modified for a DCB geometry [9, 17]. If a crack tip is loaded by a crack-tip shear force, V_o, and a crack-tip moment, M_o, the distance ahead of the crack tip at which the tractions become compressive is given by [45]

$$z_o = \frac{1}{\beta}\tan^{-1}\left\{\frac{V_o h}{h\beta M_o} + 1\right\} \ , \tag{7}$$

where $\beta = \sqrt[4]{6k/\bar{E}h^3}$, and k is the stiffness of the traction-separation law. For a DCB loaded by a point force P_∞, the crack-tip shear force is $V_o = P_\infty$, and the crack-tip moment is $M_o = P_\infty a_o$. Hence, for the geometry of this paper,

$$z_o = \frac{1}{\beta}\tan^{-1}\left\{\frac{1}{8.75h\beta} + 1\right\} \ . \tag{8}$$

It can also be shown that the cohesive-length scale for a linear traction-separation law is related to β by $\tilde{\xi}_o = 12(h\beta)^{-4}$ [17], so the length of the cohesive zone can be written as

$$\tilde{z_o} = z_o/h = 0.537\tilde{\xi}_o^{1/4}\tan^{-1}\left\{1 + 0.0614\tilde{\xi_o}^{1/4}\right\} \ . \tag{9}$$

Equation 9 has been superimposed on the plot of Fig. 12(a). Perhaps surprisingly, the equation seems to match the relationship between the cohesive-zone length, d, and the crack-tip cohesive length, ξ_o, quite well, for relatively large values of $\tilde{\xi}_o$.

In the context of Fig. 12(a), it should be noted that the ability of an elastic-foundation model to be used as an analytical description of a cohesive-zone model breaks down in the LEFM regime [46]. In particular, the equations for the elastic-foundation model do not permit any inverse-square-root description for the stresses [46]. In addition, the use of an elastic-foundation model to describe the compliance of a DCB under LEFM conditions requires a spring constant k with a limiting value of $k^* = 0.811\bar{E}/h$ [14, 17]. This

corresponds to a relatively large cohesive-length scale of $\tilde{\xi}_o = 2.5$, much in excess of a magnitude for which LEFM is valid. The elastic-foundation model does not actually provide a rigorous analytical description of a cohesive-zone model, and it is not surprising that it does not describe the cohesive-zone length at small values of $\tilde{\xi}_o$. What is, perhaps, more surprising is that the experimental observations for the length of the cohesive zone seem to be described by the $\tilde{\xi}_o^{1/4}$ relationship predicted by the elastic-foundation model at large values of $\tilde{\xi}_o$.

The root-rotation data of Fig. 8 can also be re-plotted as a function of the cohesive-length scale. This is done in Fig. 12(b). As before, the results can be compared with an analytical expression for the root rotation of a DCB with a linear traction-separation law. As shown below, this analytical result can be modified to give the LEFM result in the limit of the cohesive-length scale going to zero.

As modified for a DCB, the root rotation for a crack tip loaded by a crack-tip shear force, V_o, and a crack-tip moment, M_o, is given by [17]

$$\theta_o = 2 \times 6^{1/2} \left(\frac{\bar{E}}{hk} \right)^{1/2} \frac{V_o}{\bar{E}h} + 4 \times 6^{3/4} \left(\frac{\bar{E}}{hk} \right)^{1/4} \frac{M_o}{\bar{E}h^2} \, . \tag{10}$$

Since the root rotation corresponding to $k^* = 0.811\bar{E}/h$ is equal to the LEFM value, we can separate the effects of root rotation associated with linear elasticity from the effects associated with cohesive tractions by considering the spring constant, k, to arise from two springs in series: k^* and k_b, where k_b is the stiffness of the cohesive-law. It can then be shown that the crack-tip cohesive-length scale is related to k by

$$\tilde{\xi}_o = \frac{2\bar{E}}{k_b h} = \frac{2\bar{E}}{kh} - 2.466 \, . \tag{11}$$

Hence, an expression for the root rotation corresponding to the geometry studied in this

paper can be written as

$$\frac{\bar{E}h\theta_o}{P_\infty} = 2\times 6^{1/2}\left(0.5\tilde{\xi}_o + 1.233\right)^{1/2} + 4\times 6^{3/4}\left(0.5\tilde{\xi}_o + 1.233\right)^{1/4}\frac{a_o}{h}\,, \qquad (12)$$

using the fact that the crack-tip shear force and moment are given by $V_o = P_\infty$ and $M_o = P_\infty a_o$, respectively. This expression (with $a_o/h = 8.75$) is superimposed on the data of Fig. 12(b), showing rather remarkable agreement given the difference in cohesive laws. This agreement supports the notion that the cohesive-length scale may be a fairly general way of providing information about the compliance of the adhesive layer and the development of a cohesive zone.

3.5 Rotation and shear ahead of the crack tip

Just as the full-field capabilities of DIC allow one to explore the displacements within a cohesive zone, they also allow one to explore the rotation and shear of the adherends as a function of distance ahead of the crack tip. Unlike the earlier definition of root-rotation, in which we incorporated the effects of shear and rotation into a single description of how the centroidal axes rotate at the crack tip, here we distinguish between shear and rotation. The rotation is calculated from the DIC data for each beam as $(du/dz - dw/dx)/2$, and the shear strain as $(du/dz + dw/dx)/2$, where the co-ordinate for each beam has the z axis pointing away from the interface.

Figure 13a shows the average rotation for the beams, as a function of distance ahead of the crack. It will be observed that the rotations decay to zero well ahead of the point at which the cohesive tractions become compressive, and put the adhesive layer under a state of in-plane tension. At a load corresponding to point "D", for example, the rotation in the beams must induce an extension of about 12 μm within the adhesive over a cohesive-

zone length of about 15 mm. This would correspond to a tensile strain of approximately 8×10^{-4}. This simple estimate is consistent with results obtained in the continuum FEM results discussed in the next section.

The average shear strains (Fig. 13b) at the crack tip for this system are two orders of magnitude lower than the corresponding rotations, as expected from simple estimates. For example, the shear strain at the crack tip is expected to be approximately 5×10^{-5} for load "D". This is reasonably consistent with the experimental value, despite the relatively large uncertainties at these low strains. Perhaps not obviously, the shear strains increase in the cohesive zone ahead of the crack tip, becoming comparable to the average rotations at the location where they reach their maximum value. The numerical calculations discussed in the next section showed the same trends.

4 Comparison to numerical calculations

Previous approaches using full-field DIC techniques to extract traction-separation laws have relied on an inverse technique where the deformation in the cohesive zone is used to deduce the traction-separation law [30, 31]. Here, we have directly determined the traction-separation law, and independently measured the deformation in the cohesive zone. Therefore, it is now of interest to see how numerical predictions for the evolution of the cohesive zone compare with the experimental observations.

The numerical calculations were done using the finite-element software ABAQUS [47], implementing the cohesive zone through a user-defined element originally developed by Yang *et al.* [39, 40]. The modulus of the steel was set to be 217 GPa, corresponding to

the results of Fig. 9. The tensile portion of the traction-separation law was implemented by a six-part, piecewise-linear approximation of the measured law in Fig. 6, with an initial slope chosen to approximate an elastic modulus of 870 MPa, corresponding to the manufacturer's data sheet [48], for a 275 μm thick adhesive layer. This results in yield at about 4 MPa (corresponding to the lowest tensile tractions measured experimentally) occurring at an opening displacement of just over 1 μm (corresponding to the resolution limit of the DIC).

The significance of the compressive portion of the traction-separation law only became apparent during the analysis phase of the project, after the experimental portion had ended. In retrospect, future experiments should perhaps start with negative loads being applied until contact at the crack mouth occurs. A properly formulated cohesive-zone model, with a finite thickness for the interface [36], permits closing displacements (with an appropriate compressive stiffness) ahead of the crack. Therefore, one should be able to determine at least the initial portion of the compressive law by differentiating the J-integral with respect to the crack-tip closure.

In the absence of such experiments, numerical studies were done in the present case to explore the effect of the compressive portion of the cohesive law. It is immediately obvious from Fig. 11 that failure to incorporate compressive compliance into the traction-separation law results in an inability to capture the compressive portion of the cohesive zone. However, more significantly, numerical studies revealed that this would also result in significant errors for the predictions of the tensile portion of the cohesive zone. Indeed, the tensile portion of the cohesive-zone could be modelled correctly only by using a relatively narrow range of compressive behaviors. In the present case, we chose to describe the compressive portion of the cohesive law by assuming that it was initially anti-symmetric with respect to

the tensile portion, with yield at -4 MPa. The compressive deformation was small enough that we did not have to worry very much about the details of the strain-hardening portion, but compressive yield was required. Use of a purely elastic compressive behavior gave an incorrect description of the cohesive zone.

With the assumption that the compressive portion of the traction-separation law mirrors the tensile portion, the predictions of the development of the cohesive zone using a cohesive-zone model are shown in Fig. 14a. It will be observed that agreement with experimental results is fairly good, and close to the range one might attribute to experimental error. However, it was noted that the predictions systematically over-predicted the tensile opening. It was recognized that a cohesive-zone model does not permit the development of the in-plane tensile stress that must develop in response to the rotation of the adherends illustrated in Fig. 13a. Therefore, the calculation was repeated using a continuum model for the adhesive layer, assuming J_2-flow theory, a uniaxial constitutive law consistent with the traction-separation law of Fig. 6, and a thickness of the adhesive layer of 275 $\mu\mathrm{m}$. The results of these calculations are shown in Fig. 14b. It will be observed that the use of such a continuum model gave an even better agreement with the experimental results than the cohesive-zone model did. This indicates that the very small discrepancy in the previous figure was probably the result of approximating a thin continuum layer by a cohesive zone, and neglecting the effects of the very small in-plane tensile stresses within the adhesive (estimated from the strain quoted in the previous section to be about 0.5 MPa).

5 Conclusions

Digital-image correlation can be used to deduce an accurate mode-I traction-separation law from a double-cantilever beam in a very straight-forward fashion. The fact that displacements in beam-like geometries tend to have linear gradients can be used to improve the accuracy of the measurements, because it minimizes the introduction of spurious noise arising from digital differentiation. The traction-separation law is obtained by using DIC to obtain the rotation of the loading points and, hence, the value of the J-integral, which can then be differentiated with respect to crack-tip opening to determine the tractions.

The full-field nature of DIC can also be used to explore the concepts of root rotation, shear strains, and deformation in the cohesive zone. Furthermore, the cohesive-length scale can be measured as it evolves with loading, showing that even though LEFM behavior occurs below the resolution of the experiment, the measurements at the lowest resolvable scale are consistent with LEFM predictions. The development of the cohesive zone and the root rotation were correlated with the cohesive-length scale, and it was shown that they scale in a remarkably similar fashion to the analytical predictions of an elastic-foundation model. This suggests that the cohesive-length scale can be used as a general indication of how big a cohesive zone is, without worrying too much about the details of the traction-separation law.

The observations of the cohesive-zone development illustrate the importance of including a compressive regime in cohesive laws. The use of a cohesive-zone model incorporating the measured traction-separation law and an appropriate compressive regime gave very good predictions for the deformation ahead of the crack tip, although there was a small error attributed to the fact that a cohesive-zone model doesn't allow for the development of

in-plane stresses. Our method allows one to describe the deformation of a cohesive zone, and the technique is probably rather more direct than those using inverse methods to deduce the traction-separation laws from the deformation itself.

Acknowledgements

This work was supported in part by the Department of Energy under Award Number DE-PI0000012. JMG acknowledges the support of the DoD in the form of a SMART scholarship. MDT acknowledges support from the Janine Johnson Weins Endowed Professorship Fund at the University of Michigan, an Overseas Fellowship at Churchill College, and the hospitality of Prof. Norman Fleck during a sabbatical leave at Cambridge University. The authors also acknowledge useful discussions with Prof. Ellen Arruda during the course of this study.

References

[1] J. W. Obriemoff. The splitting strength of mica. *Proceedings of the Royal Society of London*, 127A:290–297, 1930.

[2] B.F. Sørensen, A. Horsewell, O. Jørgensen, A.N. Kumar and P. Engbæk. Fracture resistance measurement method for in situ observation of crack mechanisms. *Journal of the American Ceramic Society*, 81:661–669, 1998.

[3] B. F. Sørensen, K. Jørgensen, T. K. Jacobsen and R. C. Østergaard. DCB-specimen loaded with uneven bending moments. *International Journal of Fracture*, 141:163–176, 2006.

[4] ASTM. *Standard Test Method for Fracture Strength in Cleavage of Adhesives in Bonded Metal Joints*, D3433-99 (2012) edition.

[5] ASTM. *Standard Test Method for Mode I Interlaminar Fracture Toughness of Unidirectional Fiber-Reinforced Polymer Matrix Composites*, D5528-13 (2013) edition.

[6] British Standard. *Determination of the mode I adhesive fracture energy G_{IC} of structure adhesives using the double cantilever beam (DCB) and tapered double cantilever beam (TDCB) specimens*, BS 7991:2001 edition.

[7] P. P. Gillis and J. J. Gilman. Double-cantilever cleavage mode of crack propagation. *Journal of Applied Physics*, 35:647–658, 1964.

[8] S. Mostovoy, P. B. Crosley and E. J. Ripling. Use of crack-line-loaded specimens for measuring plane-strain fracture toughness. *Journal of Materials*, 2:661–681, 1967.

[9] M. F. Kanninen. Augmented double cantilever beam model for studying crack propagation and arrest. *International Journal of Fracture*, 9:83–92, 1973.

[10] S. M. Wiederhorn, A. M. Shorband and R. L. Moses. Critical analysis of the theory of the double cantilever method of measuring fracture surface energy. *Journal of Applied Physics*, 39:1569–1572, 1968.

[11] J. G. Williams. End corrections for orthotropic DCB specimens. *Journal of Composite Science and Technology*, 35:367–376, 1989.

[12] Z. Suo, G. Bao, B. Fan and T. C. Wang. Orthotropy rescaling and implications for fracture in composites. *International Journal of Solids and Structures*, 28:235–248, 1991.

[13] C. T. Sun and R. K. Pandey. Improved method for calculating strain energy release rate based on beam theory. *AIAA Journal*, 32:184–189, 1994.

[14] S. Li, J. Wang and M. D. Thouless. The effects of shear on delamination of beam-like geometries. *Journal of the Mechanics and Physics of Solids*, 52:193–214, 2004.

[15] J. Wang and P. Qiao. Mechanics of bimaterial interface: Shear deformable split bilayer beam theory and fracture. *Journal of Applied Mechanics*, 72:674–682, 2005.

[16] M. G. Andrews and R. Massabò. The effects of shear and near tip deformations on energy release rate and mode mixity of edge-cracked orthotropic layers. *Engineering Fracture Mechanics*, 74:2700–2720, 2007.

[17] M. D. Thouless. Shear forces, root rotations, phase angles and delamination of layered materials. *Journal of Engineering Fracture Mechanics*, 191:153–167, 2018.

[18] U. Vilks V. Tamuzs, S. Tarasovs. Delamination properties of translaminar-reinforced composites. *Composites Science and Technology*, 63:1423–1431, 2003.

[19] M. F. S. F. de Moura, J. J. L. Morais and N. Dourado. A new data reduction scheme for mode I wood fracture characterization using the double cantilever beam test. *Engineering Fracture Mechanics*, 75:3852–3865, 2008.

[20] W. Xu and Z. Z. Guo. A simple method for determining the mode I interlaminar fracture toughness of composites without measuring the growing crack length. *Journal of Engineering Fracture Mechanics*, 191:476–485, 2018.

[21] J. G. Williams. Large displacement and end block effects in the DCB interlaminar test in modes I and II. *Journal of Composite Materials*, 21:330–347, 1987.

[22] A. J. Paris and P. C. Paris. Instantaneous evaluation of J and C^*. *International Journal of Fracture*, 38:R19–R21, 1988.

[23] P. Olsson and U. Stigh. On the determination of the constitutive properties of thin interphase layers - an exact solution. *International Journal of Fracture*, 41:R71–R76, 1989.

[24] V. C. Li, C. M. Chan and Leung C. K. Y. Experimental determination of the tension-softening relations for cementitious composites. *Cement and Concrete Research*, 17:441–452, 1987.

[25] J. D. Gunderson, J. F. Brueck and A. J. Paris. Alternative test method for interlaminar fracture toughness of composites. *International Journal of Fracture*, 143:273–276, 2007.

[26] C. K. Desai, S. Basu and V. Parameswaran. Determination of traction separation law for interfacial failure in adhesive joints at different loading rates. *The Journal of Adhesion*, 92:819–839, 2016.

[27] S. Rajan, M. A. Sutton, R. Fuerte and A. Kidane. Traction-separation relationship for polymer-modified bitumen under mode I loading: Double cantilever beam experiment with stereo digital image correlation. *Engineering Fracture Mechanics*, 187:404–421, 2018.

[28] W. H. Peters, W. F. Ranson, M. A. Sutton, T. C. Chu and J. Anderson. Application of digital correlation methods to rigid body mechanics. *Optical Engineering*, 22:738–742, 1983.

[29] M. A. Sutton, M. Cheng, W. H. Peters, Y. J. Chao and S. R. McNeill. Application of an optimized digital correlation method to planar deformation analysis. *Image and Vision Computing*, 4:143–150, 1986.

[30] B. Shen and G.H. Paulino. Direct extraction of cohesive fracture properties from digital image correlation: A hybrid inverse technique. *Experimental Mechanics*, 51:143–163, 2011.

[31] B. Blaysat, J.P.M. Hoefnagels, G. Lubineau, M. Alfano and M.G.D. Geers. Interface debonding characterization by image correlation integrated with double cantilever beam kinematics. *International Journal of Solids and Structures*, 55:79–91, 2015.

[32] T. Zhu, K. M. Liechti and K. Ravi-Chandar. Direct extraction of rate-dependent traction-separation laws for polyurea/steel interfaces. *International Journal of Solids and Structures*, 46:31–51, 2009.

[33] C. Wu, S. Gowrishankar, R. Huang and K. M. Liechti. On determining mixed-mode traction-separation relations for interfaces. *International Journal of Fracture*, 202:1–19, 2016.

[34] R. B. Sills and M. D. Thouless. The effect of cohesive-law parameters on mixed-mode fracture. *Engineering Fracture Mechanics*, 109:353–368, 2013.

[35] R. B. Sills and M. D. Thouless. Cohesive-length scales for damage and toughening mechanisms,. *International Journal of Solids and Structures*, 55:32–43, 2015.

[36] J. P. Parmigiani and M. D. Thouless. The effects of cohesive strength and toughness on mixed-mode delamination of beam-like geometries. *Engineering Fracture Mechanics*, 74:2675–2699, 2007.

[37] A. Hillerborg, M. Modéer and P.-E. Petersson. Analysis of crack formation and crack growth in concrete by means of fracture mechanics and finite elements. *Cement and Concrete research*, 6:773–782, 1976.

[38] A. Needleman. A continuum model for void nucleation by inclusion debonding. *Journal of Applied Mechanics*, 54:525–531, 1987.

[39] Q. D. Yang, M. D. Thouless and S. M. Ward. Numerical simulations of adhesively-bonded beams failing with extensive plastic deformation. *Journal of the Mechanics and Physics of Solids*, 47:1337–1353, 1999.

[40] Q. D. Yang and M. D. Thouless. Mixed-mode fracture analyses of plastically-deforming adhesive joints. *International Journal of Fracture*, 110:175–187, 2001.

[41] G. Bao, S. Ho, Z. Suo and B. Fan. The role of material orthotropy in fracture specimens for composites. *International Journal of Solids and Structures*, 29:1105–1116, 1992.

[42] C. Liu, P. J. Rae, C. M. Cady and M. L. Lovato. Damage and fracture of high-explosive mock subject to cyclic loading. In T. Proulx, editor, *Mechanics of Time-Dependent Materials and Processes in Conventional and Multifunctional Materials*, volume 3 of *Conference Proceedings of the Society for Experimental Mechanics Series*, pages 151–157. Springer, New York, NY, USA, 2011.

[43] J Réthoré, S. Roux and F. Hild. From pictures to extended finite elements: extended digital image correlation (X-DIC). *Comptes rendus - Mécanique*, 335:131–137, 2007.

[44] J Réthoré, F. Hild and S. Roux. Shear-band capturing using a multiscale extended digital image correlation technique. *Computational Methods Applied Mechanics Engineering*, 196:5016–5030, 2007.

[45] J. R. Barber. *Intermediate Mechanics of Materials*. Springer, Dordrecht, The Netherlands, 2011.

[46] H. Wang, W. Lu, J. R. Barber and M. D. Thouless. The roles of cohesive strength and toughness for crack growth in visco-elastic and creeping materials. *Engineering Fracture Mechanics*, 160:226–237, 2016.

[47] *ABAQUS version 6.14-1, 2014. User Documentation, Dassault Systems.*, 2014.

[48] Dow Automotive Systems. *Total Solutions for Commercial Transportation*. http://msdssearch.dow.com/PublishedLiteratureDOWCOM/dh_0894/0901b8038089473e.pdf (accessed March 13, 2018).

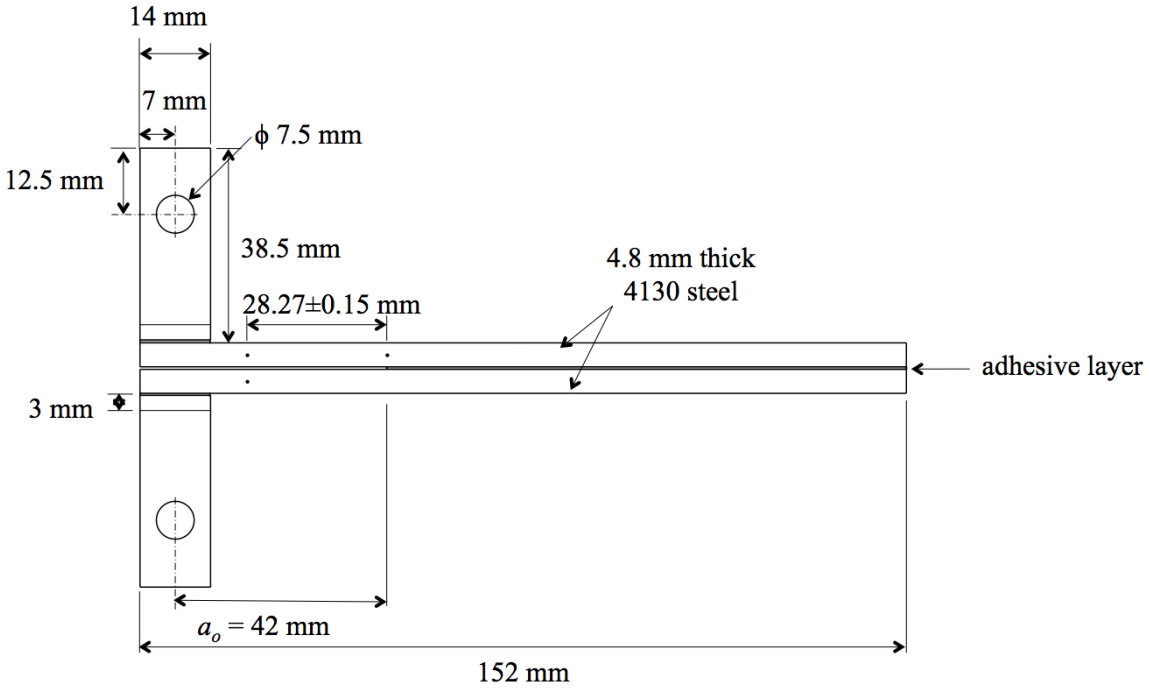

Figure 1: The double-cantilever beam geometry used in these studies. The adherends are made of a 4130 steel, bonded by a two part, structural adhesive (Dow Betamate® 73326M/733327M).

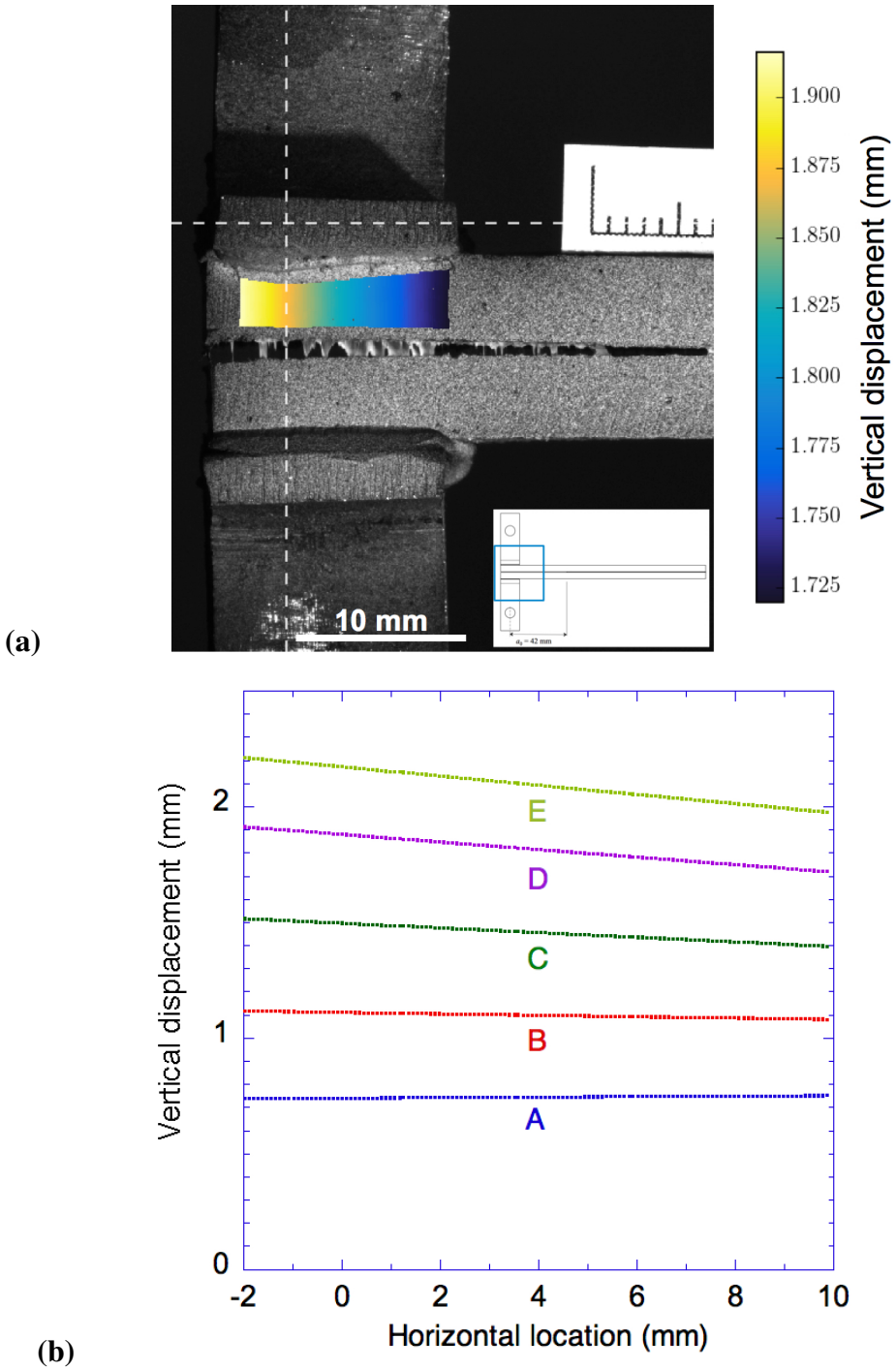

Figure 2: Calculation of the relative rotation between the loading points. The digital image in **(a)** shows a color map containing vertical displacement data for one beam, corresponding to approximately 4000 points. All these data taken for one particular load collapse onto a single line, as shown in **(b)** for five specific loads "A"-"E" (defined later). This type of plot confirms the well-defined rotation at the point of loading for each beam. The origin and co-ordinate system for this plot are shown in (a).

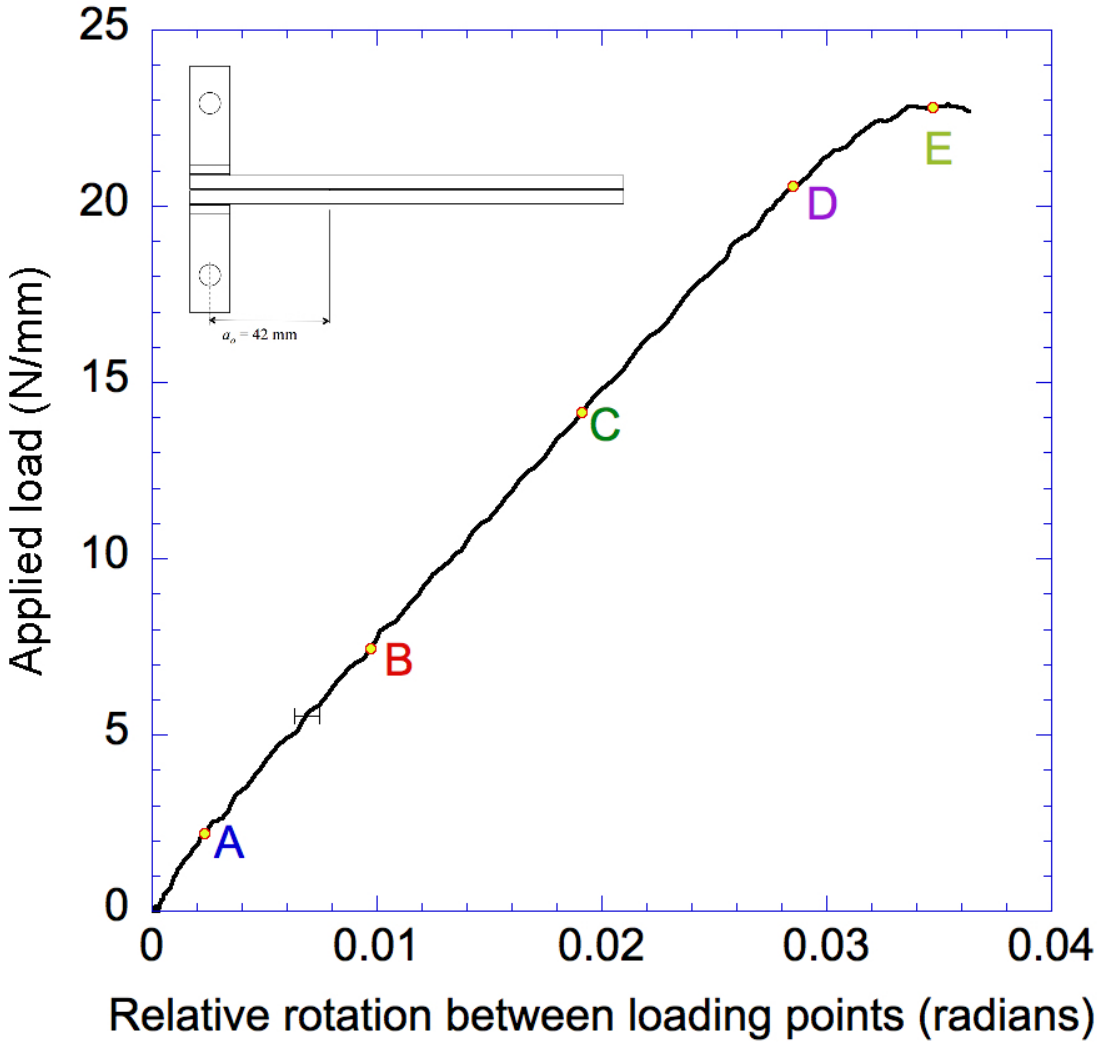

Figure 3: A plot of the applied load against the relative rotation between the two loading points. The specific loads ("A"-"E") referenced throughout this paper are identified in this plot.

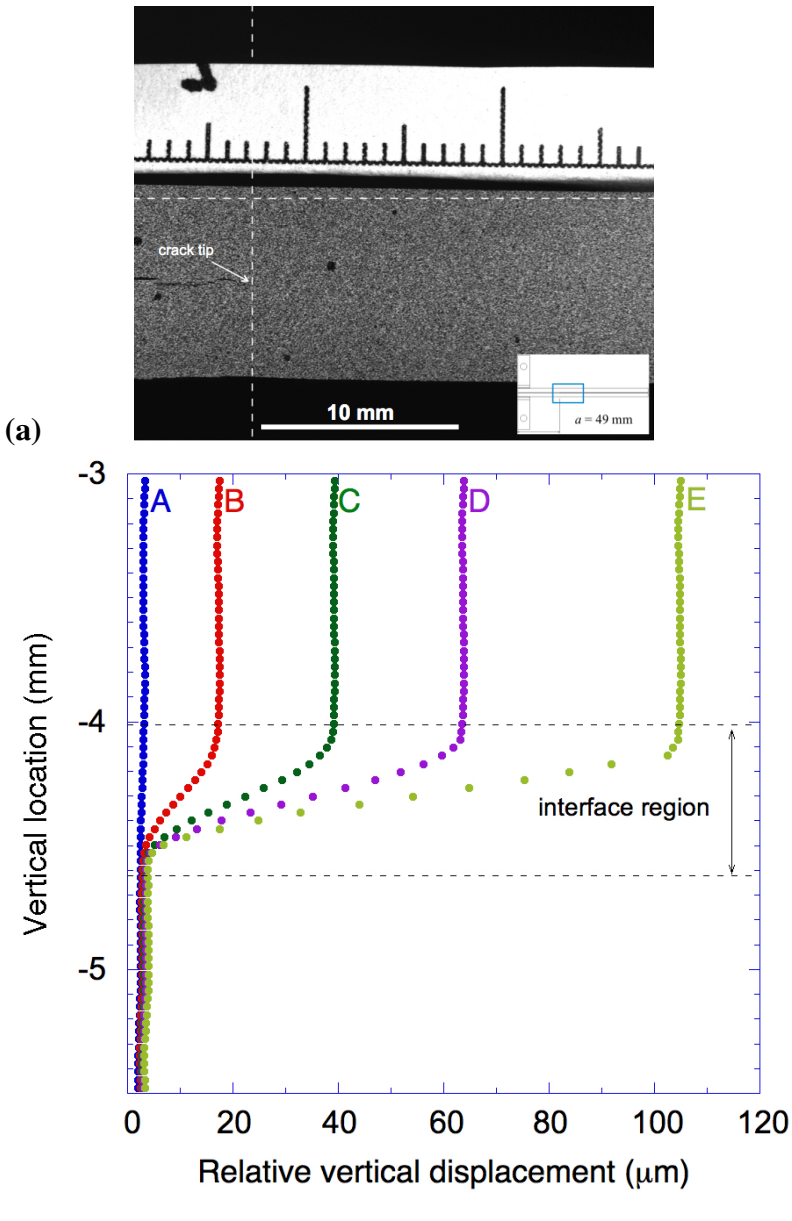

Figure 4: Calculation of the crack-tip opening. **(a)** Shows an image of the crack-tip region, the origin of a co-ordinate system for (b), and vertical axis through what has been identified as the crack tip. **(b)** Shows a plot of the relative vertical displacements along this axis, as a function of vertical position. The dotted lines indicate the interface region over which the measurements transitioned between those in the adhesive and those in the steel. The thickness of this region is significantly larger than the actual thickness of the adhesive layer, which was 250-300 μm. The lines "A"-"E" correspond to the measurements taken at the loads identified in Fig. 3.

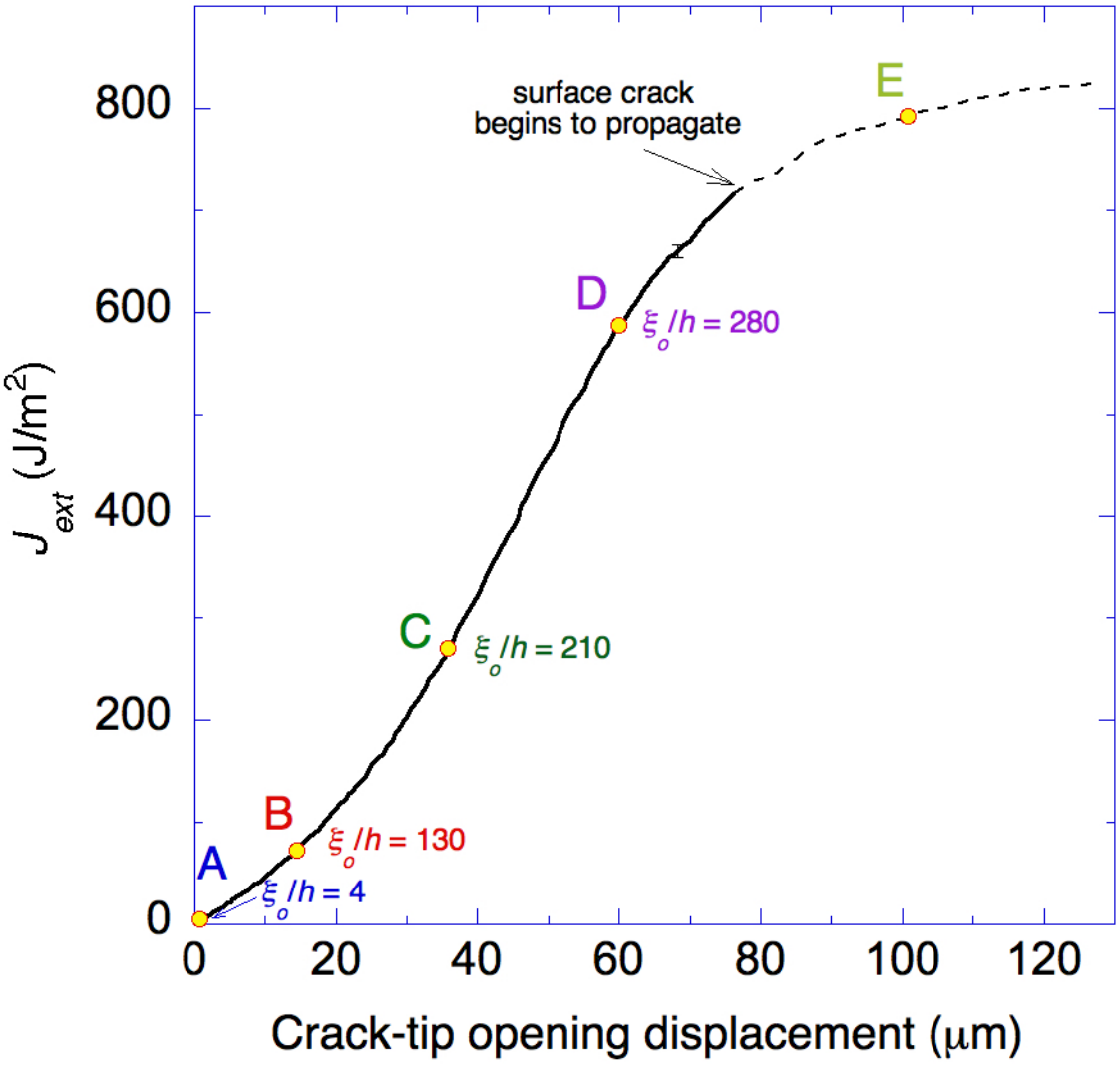

Figure 5: The J-integral was computed as the product of the applied load and the relative rotation between the loading points (Fig. 3). This figure presents these values plotted against the corresponding crack-tip opening displacement (obtained from data such as those shown in Fig. 4). The points corresponding to the specific loads ("A"-"E") have been identified. The associated crack-tip cohesive-length scales were calculated from the appropriate values of the J-integral, opening displacement, and a Young's modulus taken to be 217 GPa (as calculated from the data shown in Fig. 9). It is noted that the surface crack began to propagate at a load between "D" and "E". The fact that the J-integral was still rising at this stage indicates that the crack was not advancing elsewhere within the specimen. However, the appropriate value of the opening displacement may be ambiguous after this point.

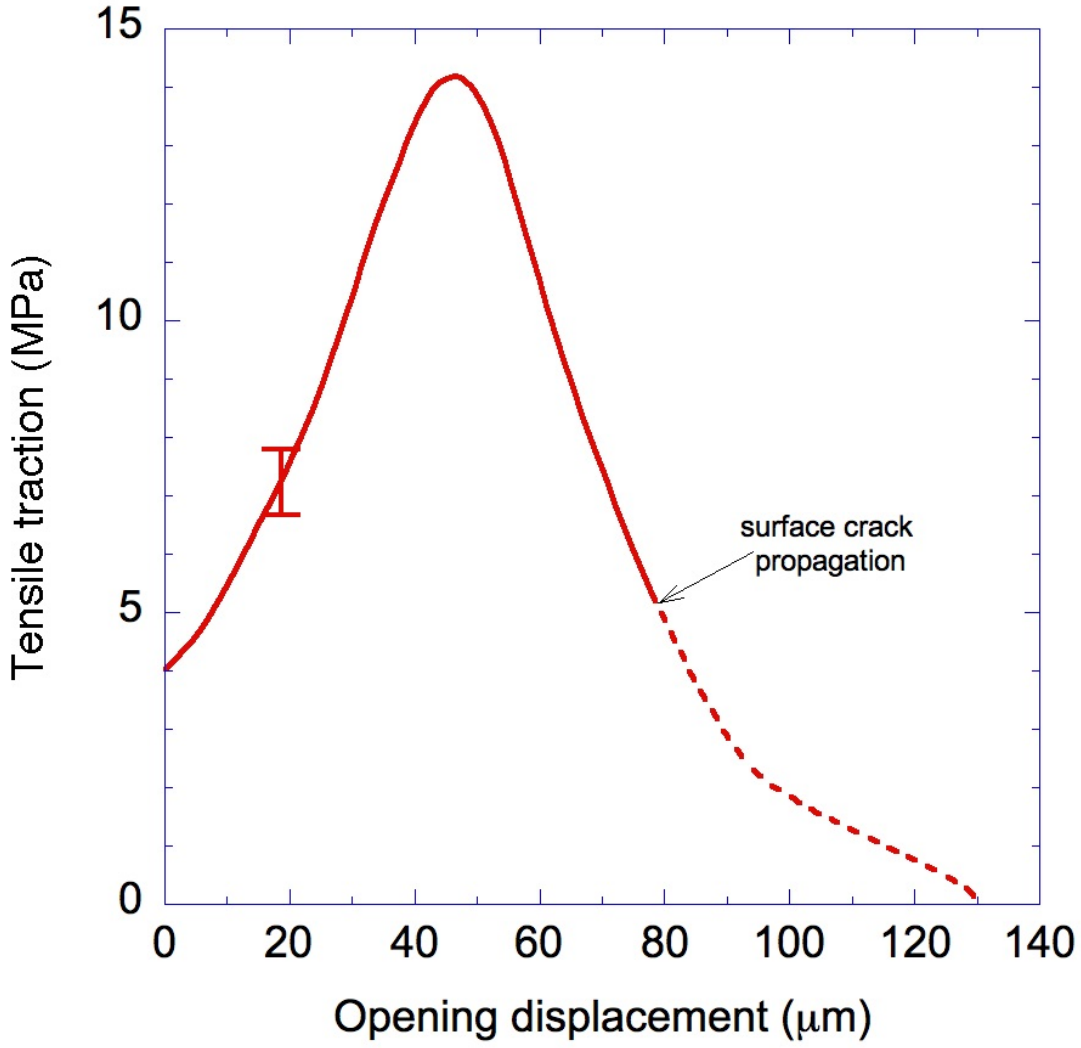

Figure 6: Traction-separation law obtained by differentiation of a curve fit to the data in Fig. 5. The error bar shown in this figure includes the effects of different differentiation schemes.

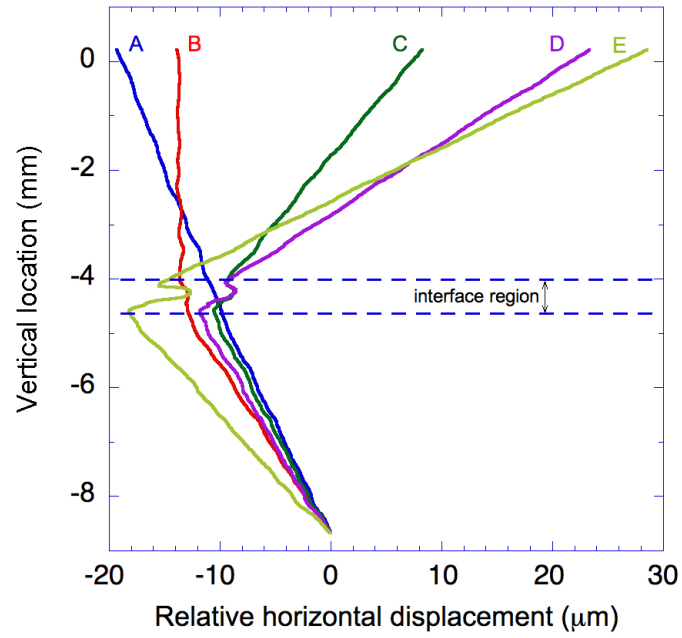

(a)

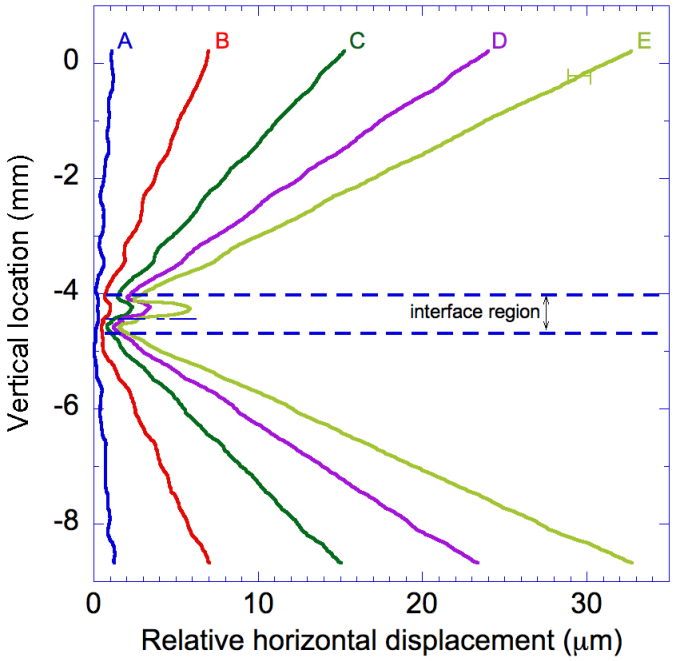

(b)

Figure 7: **(a)** Plots of the relative horizontal displacement as a function of vertical location at the crack tip for the specific loads "A"-"E", as identified in Fig. 3, and using the coordinate system shown in Fig. 4(a). These are not corrected for the rigid-body rotations that develop during loading. **(b)** The data re-plotted after correction for rigid-body rotations. The reference point for zero displacement is now the point defined by the intersection of the extrapolated lines, as indicated by the dashed line within the interface region.

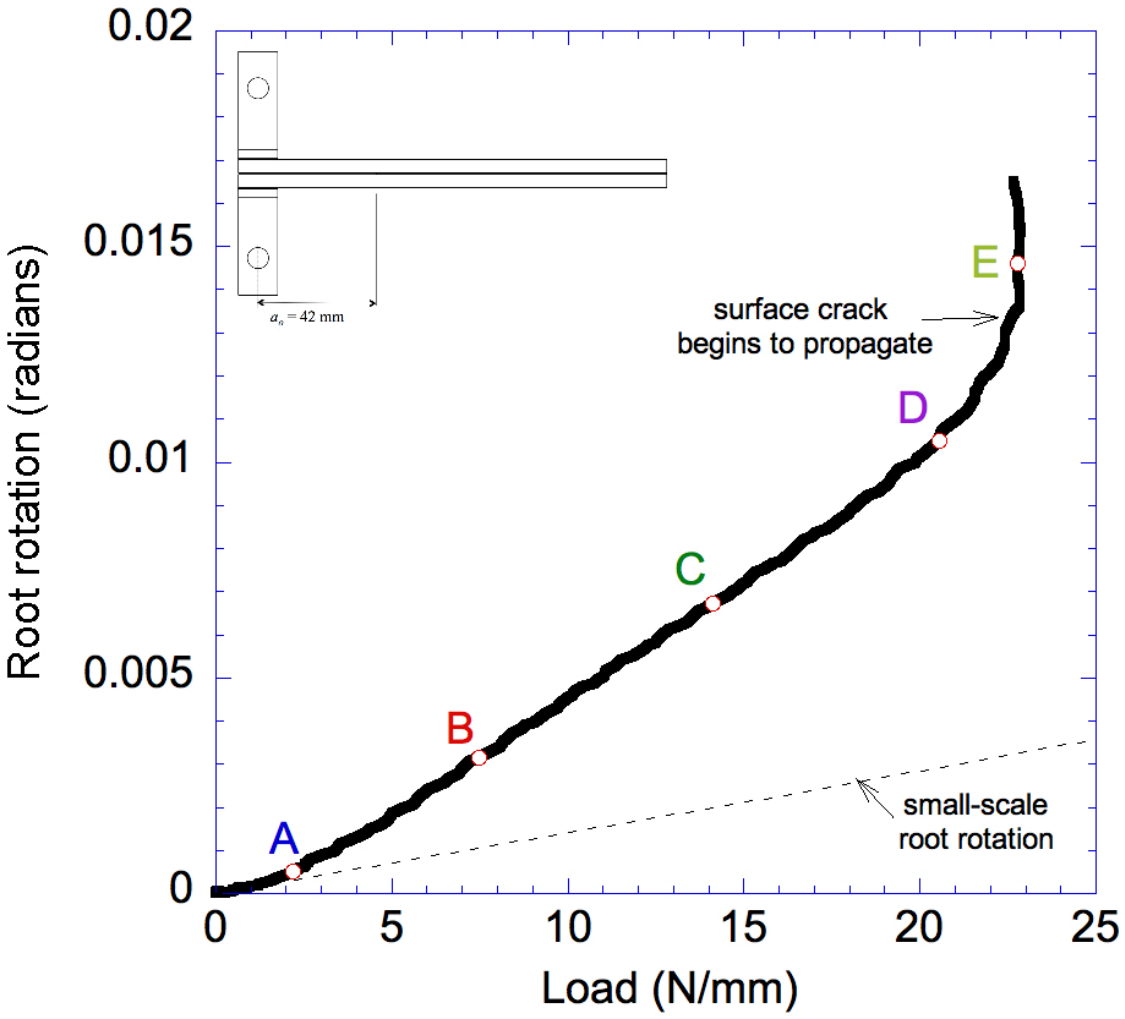

Figure 8: The root rotation, defined as the sum of $\partial u/\partial z$ for both arms (with the z-axis pointing away from the interface in both arms), as a function of load. Superimposed on this plot is the calculated small-scale root rotation corresponding to the specific geometry of this paper, and a Young's modulus of 217 GPa.

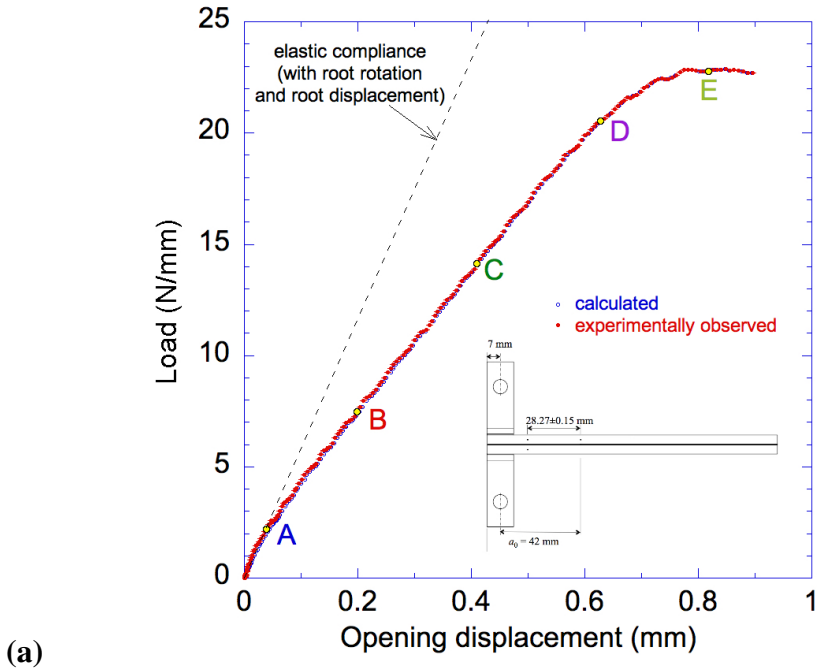

(a)

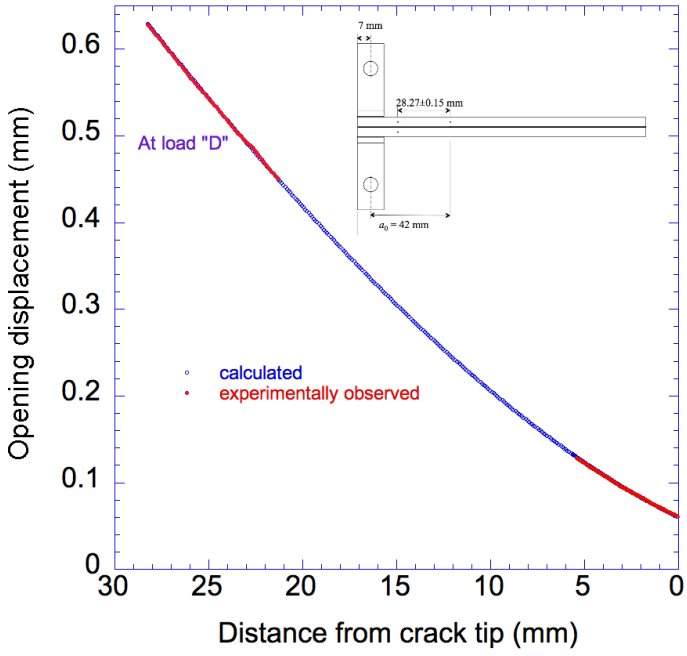

(b)

Figure 9: **(a)** Comparison between the calculated and experimental opening displacements at a point 28.3 mm behind the crack tip, assuming an effective modulus of 217 GPa. These calculations were done assuming an Euler beam acted upon by the appropriate load and moment at the point of interest, and assuming the root rotation given in Fig. 8. **(b)** A plot showing how the deformation of the centroidal axis is described by an Euler-beam description along its whole length, with an appropriate root rotation and root displacement at the crack tip.

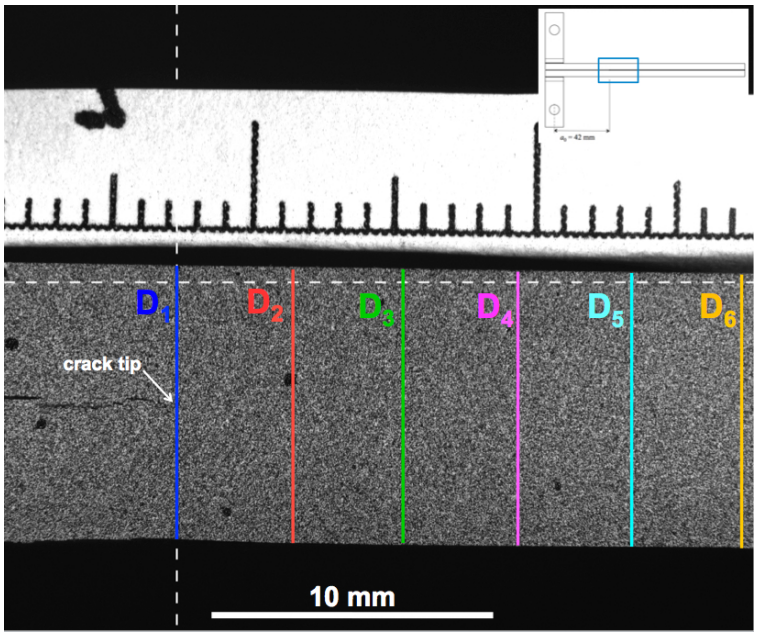

(a)

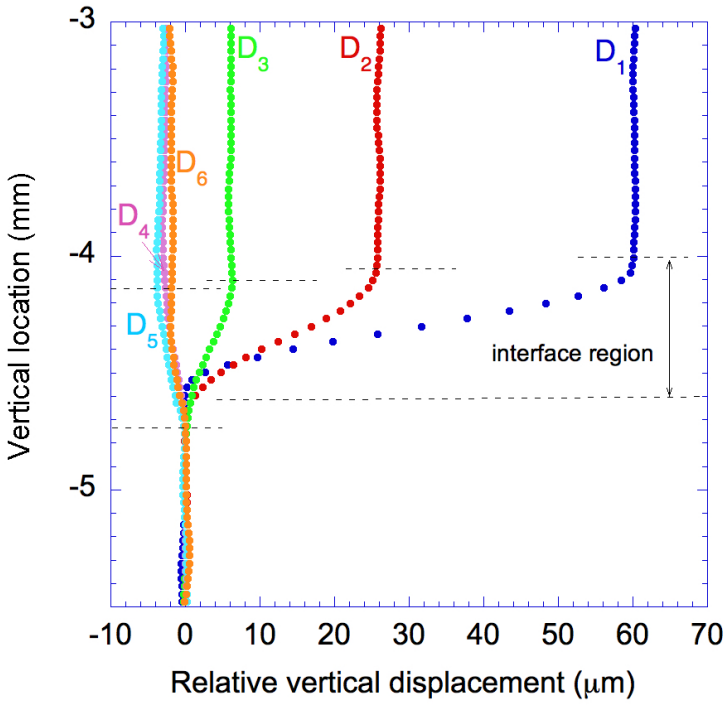

(b)

Figure 10: **(a)** Example of lines along which normal displacements are measured as a function of vertical distance. The origin and crack tip are illustrated in this figure. **(b)** The results for the six specific lines shown in (a). The origin for the vertical location is indicated by the dashed line in (a).

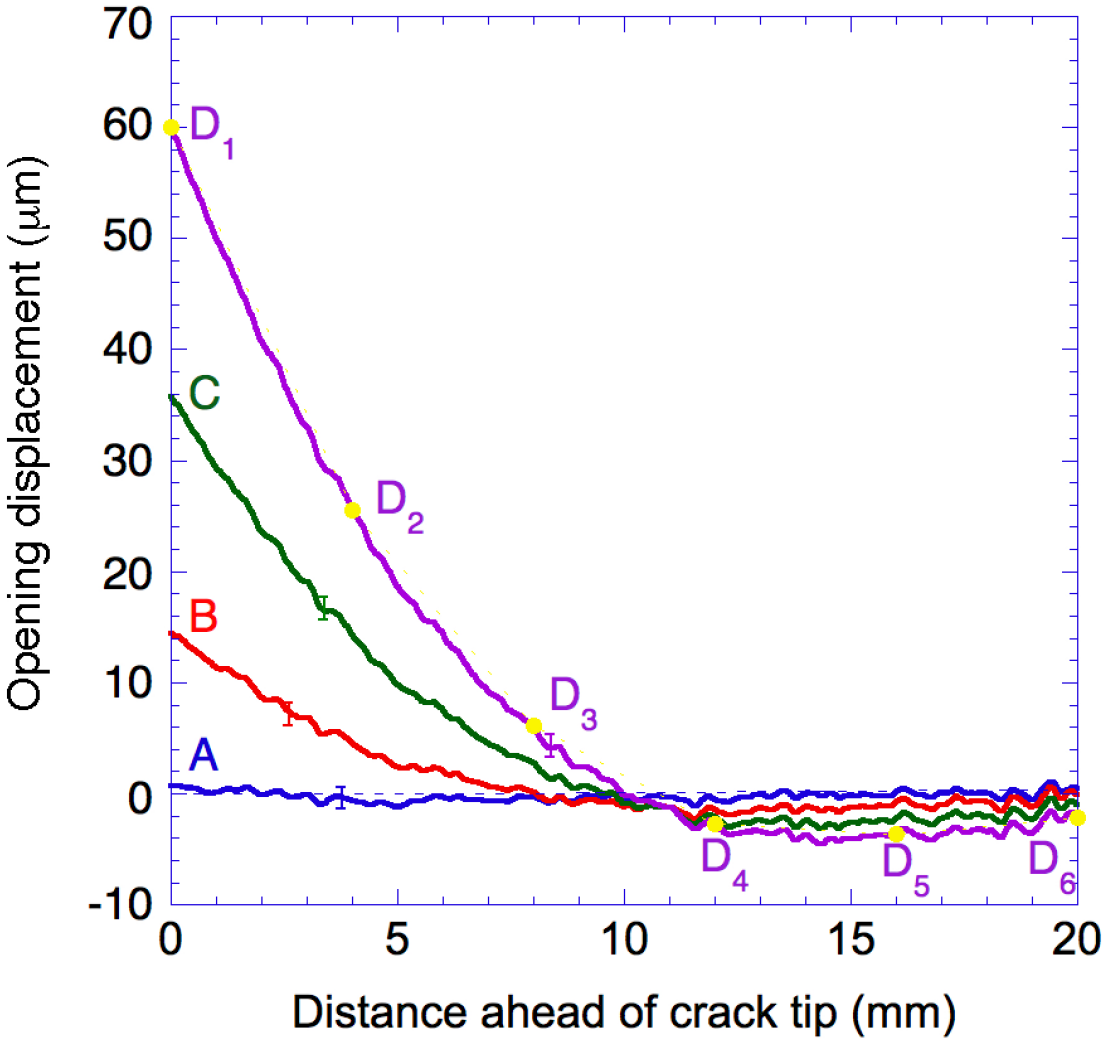

Figure 11: Plot of normal displacements ahead of the crack tip using the data obtained as shown in Fig. 4. The four lines correspond to the loads "A"-"D" indicated in Fig. 3.

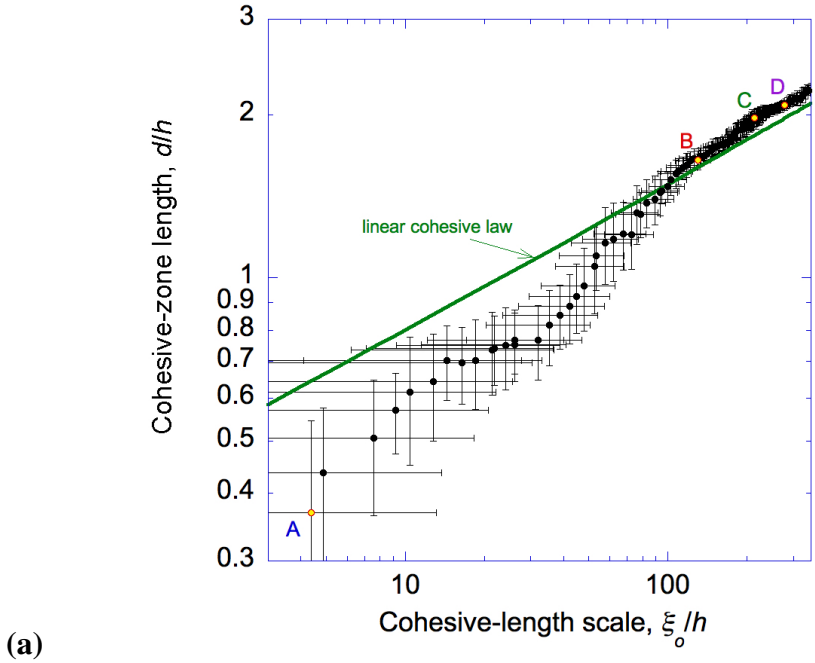

(a)

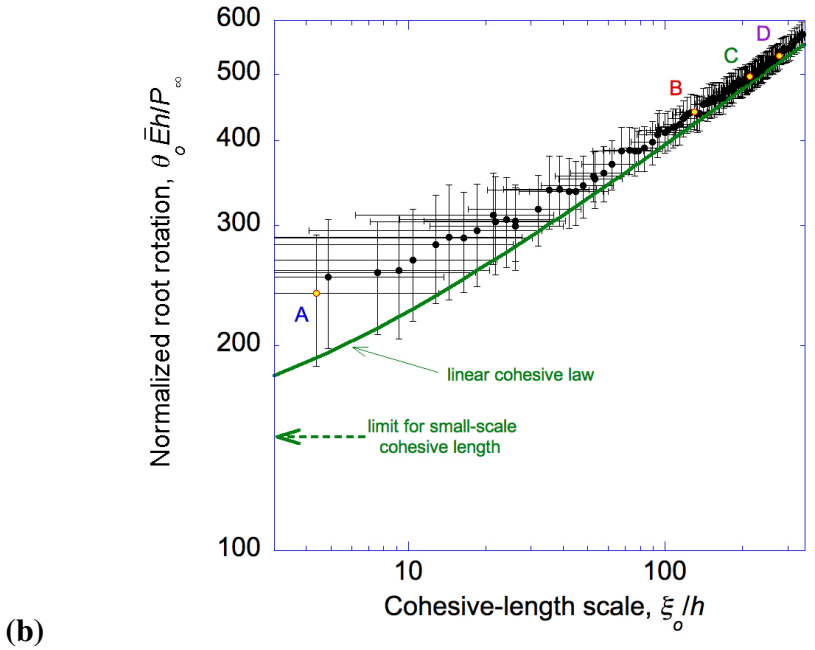

(b)

Figure 12: **(a)** A comparison between the "length" of the cohesive zone, defined as the distance from the cohesive-crack tip to the point at which the tractions become compressive, and the cohesive-length scale. **(b)** A plot of how the root rotation varies with cohesive-length scale. Also plotted on these figures are comparisons to the results for an elastic-foundation model.

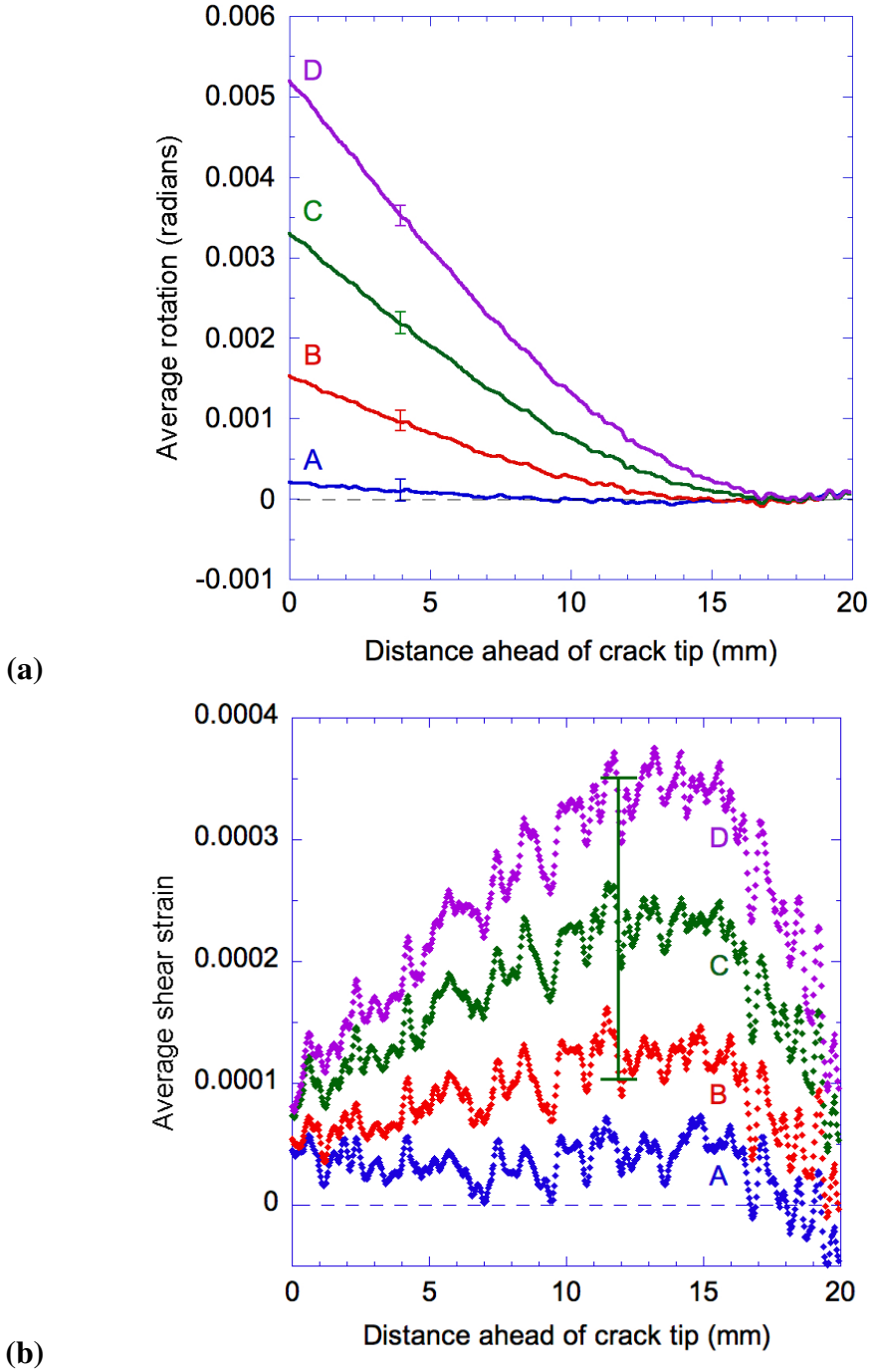

Figure 13: Plots of **(a)** average rotation and **(b)** shear strain ahead of crack tip. A representative error bar is shown in (b) that applies to all four plots.

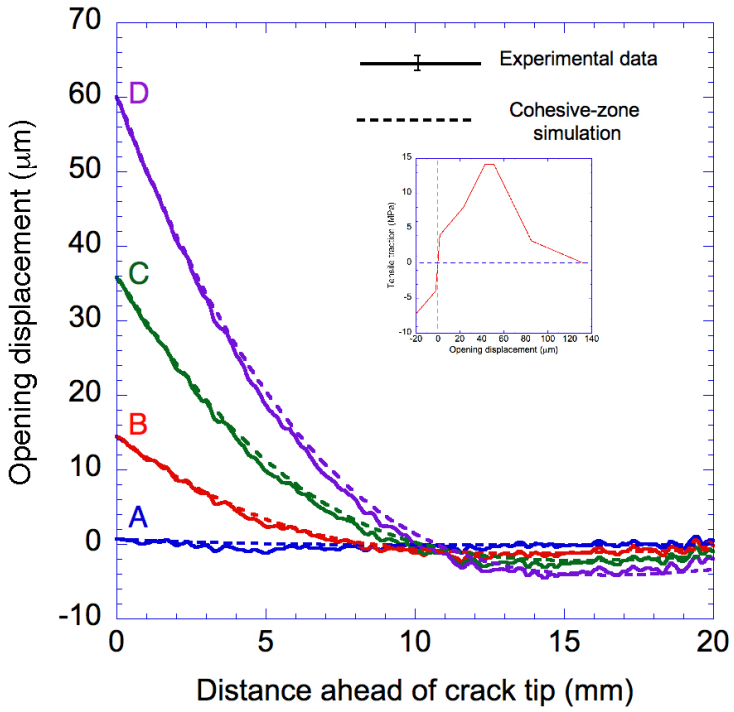

(a)

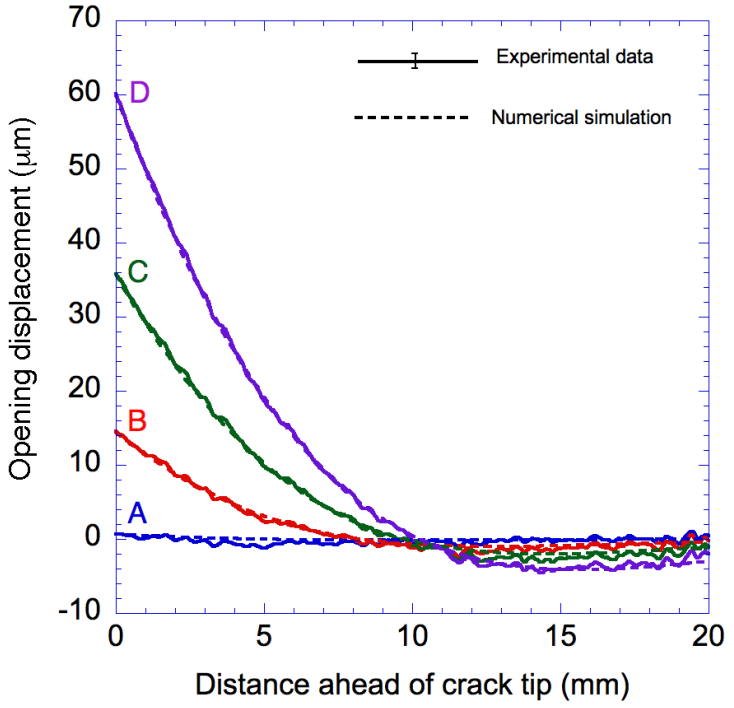

(b)

Figure 14: A comparison between the experimental observations of opening displacements with numerical predictions based on **(a)** a cohesive-zone model (see inset), and **(b)** a continuum model of the adhesive, assuming J_2-flow theory and a constitutive law identical to the traction-separation law used for (a).